Electronic Supplementary Material (ESI) for ChemComm.

Electronic Supplementary Information (ESI):

A facile strategy for the fast construction of porous graphene frameworks and their enhanced electrosorption performance

Haiyan Duan, Tingting Yan, Guorong Chen, Jianping Zhang, Liyi Shi and Dengsong Zhang*

Research Center of Nano Science and Technology, Shanghai University, Shanghai 200444, China.

Fax: 86 21 66136079; E-mail: dszhang@shu.edu.cn

1. Materials and Methods

1.1 Materials

Colloidal silica and triarylsufonium hexafluoroantimonate salts (50wt% in propylene carbonate) were purchased from Sigma Aldrich. 3-(trimethoxysilyl)propylmethacrylate (MPS) was provided by Aladdin. Epoxy acrylate resin (EA) were purchased from Nanjing fine chemical co. LTD, 1,4-butanediol diglycidyl ether (BDDGE) was purchased from TOKYO KASEI. Other chemicals were supplied by Sinopharm Chemical Reagent Company. All chemicals were used without further purification except colloidal silica. Before preparation, the colloidal silica was dialyzed in methanol solution and then modified by MPS under ultrasonication for 1h. Deionized water was used throughout the process.

1.2 Preparation

Briefly, 3.0 g of ferrocene was thoroughly mixing with 1.36 g of the mixture of EA and BDDGE (mass ratio: 1.4) and then 5.64 g of modified silica was added. After ultrasonication for ~30 min, 0.06 g of triarylsufonium hexafluoroantimonate salts was added and the mixture was left to evaporate at room temperature to remove solvent. After UV irradiation directly in few seconds, nanocomposites were obtained. The nanocomposites were directly calcinated under argon atmosphere at 400 ^{o}C for 2 h, then at 1200 ^{o}C for 2 h. The SiO_2 templates and Fe species were removed firstly by 40 wt.% HF solution then by 2M HCl solution to obtain PGF.

For comparision, the porous graphene frameworks calcinated at lower temperature of 1000 ^{o}C (denoted as PGF-LT) and higher temperature of 1400 ^{o}C (denoted as PGF-HT) were also prepared. The porous carbon (denoted as MC-NF) was developed by pyrolysis nanocomposites without ferrocene, and the carbon (denoted as Carbon-NS) was also prepared by pyrolysis without colloidal silica.

1.3 Characterization and electrochemical measurements

The morphologies were observed using transmission electron microscopy (TEM, JEOL JEM-200 CX). High-Resolution TEM (HRTEM) images were obtained using a JEOL JEM-2010F instrument. Raman spectra were taken on a JY H800UV spectrometer. N_2 adsorption-desorption measurements were conducted using an Autosorb-IQ2, Quantachrome Corporation at 77 K. The Brunauer-Emmett- Teller method was utilized to calculate the specific surface area and the pore volumes, the pore size distributions were derived from the adsorption branches of the isotherms using quenched solid density functional theory (QSDFT). The X-ray photoelectron spectroscopy (XPS) was recorded on a Perkin-Elmer PHI 5000C ESCA system equipped with a dual X-ray source, using a 45 Mg Kα (1253.6 eV) anode and a hemispherical energy analyser.

The electrosorption electrodes were fabricated by mixing 10 wt% of polytetrauoroethylene and 90 wt% of the active component homogenously in ethanol. The as-obtained slurry was then pressed onto graphite substrate and dried at above 110 ^{o}C. The cyclic voltammetry (CV) and electrochemical impedance spectroscopy (EIS) were performed on a CHI 660D and the galvanostatic charge-discharge (GCD) tests were carried out using an automatic LAND battery test instrument. All of the electrochemical experiments were measured using a three-electrode cell configuration in a 0.5 M NaCl solution that consisted of active materials as the working electrode, graphite as the counter electrode, and saturated calomel electrode as the reference electrode, respectively. The specific capacitances C_s were calculated from the following equation:

$$C = (\int I\, dV)/2 v m \Delta V \qquad (1)$$

where C is the specific capacitance, I the response current, ΔV the potential window, v the potential scan rate and m the mass of active material.

1.4 Electrosorptive experiments

The electrosorptive experiments were performed in a flow through recycling cell included two sided electrodes with a total active mass of 160 mg and a size of 60 mm × 70 mm × 0.2 mm. In each electrosorptive experiment, the NaCl solution with a total volume of 35 mL was continuously pumped to the electrosorption cells using a pump at a flow rate of 40 mL min^{-1} and salt ions were adsorbed by applying an external voltage. The NaCl solution with the beginning concentration of 100, 300, and 500 mg L^{-1} were utilized respectively. The applied voltage ranges from 1.0 to 1.4 V with an interval of 0.2 V. The concentration change of the solution was monitored transiently and measured at the outlet of the cell by a conductivity meter. Herein, the salt adsorption capacity SAC of electrodes was calculated according to the following equation:

$$SAC = (C_0 - C)V/m \qquad (2)$$

Where C_0 and C are the initial and final concentrations of NaCl solution, V is the total volume of NaCl solution, and m is the total mass of active components in two working electrodes.

The salt adsorption rate, *SAR*, of the electrodes was obtained from the formulas:

$$SAR = SAC/t \qquad (3)$$

where *SAR* is the salt adsorption rate, *SAC* is the salt adsorption capacity, and t is the adsorption time.

Charge efficiency (Λ) is a functional tool to gain insight into the electric double layer formed at the interface between the electrode and the solution, which reflects the ratio between the amounts of removed salt ions and electrical charge, which is obtained according to the following equation:

$$\Lambda = F \times \Gamma/\Sigma \qquad (4)$$

where F is the Faraday constant (96485 C mol^{-1}), Γ is the salt adsorption capacity (mol g^{-1}) and Σ (charge, C g^{-1}) is obtained by integrating the corresponding current.

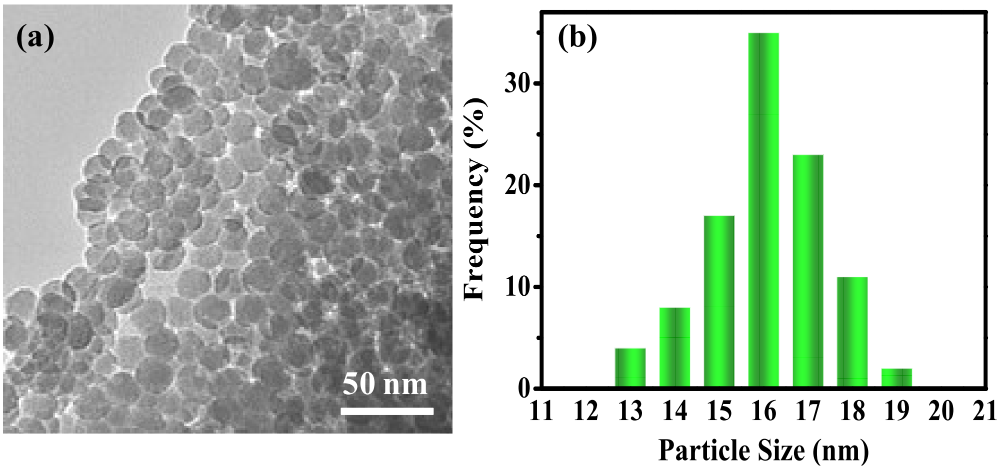

Fig. S1 TEM images and the corresponding particle size distribution histograms of silica-16nm.

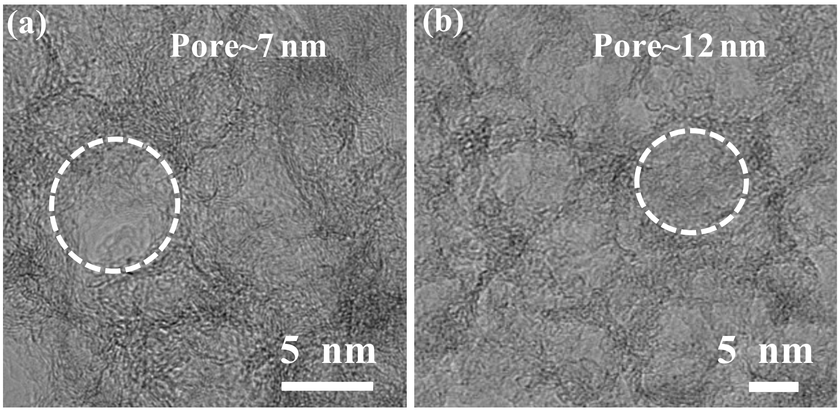

Fig. S2 HRTEM images of (a) PGF with pore size of 7 nm and (b) PGF with pore size of 12 nm.

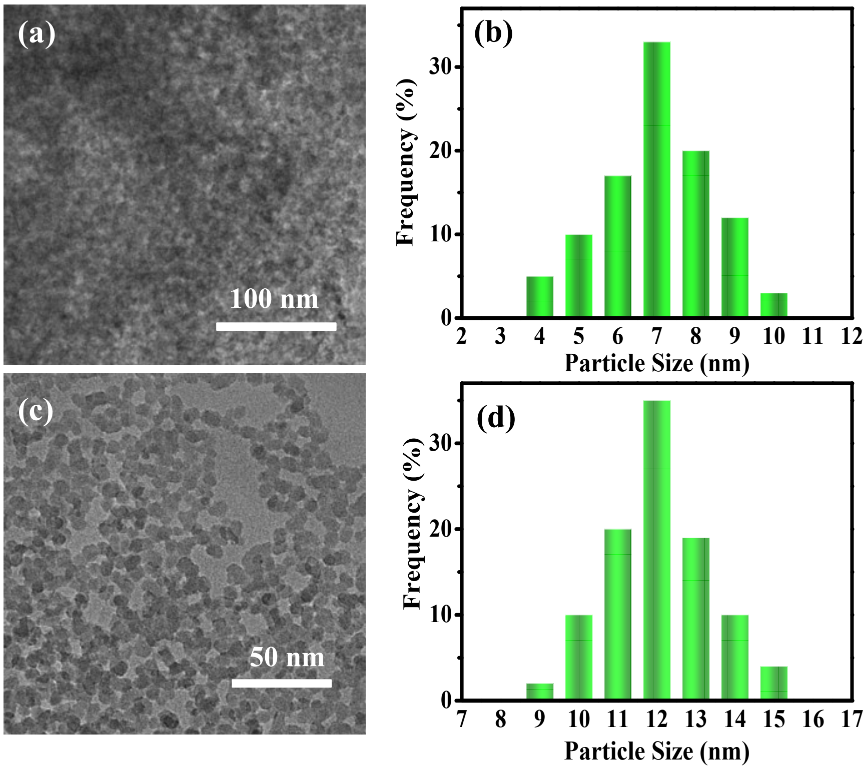

Fig. S3 TEM images and the corresponding particle size distribution histograms of (a,b) silica-7nm and (c,d) silica-12nm.

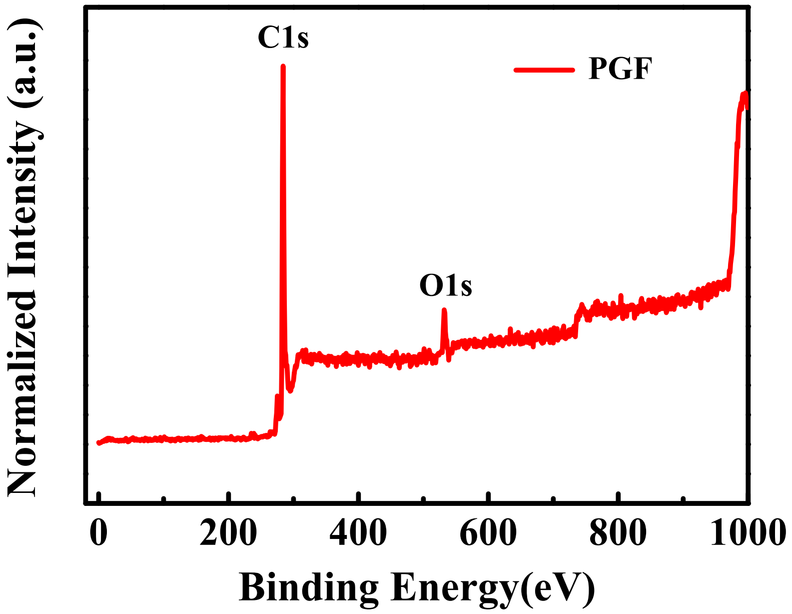

Fig. S4 XPS spectra of the PGF (survey scan).

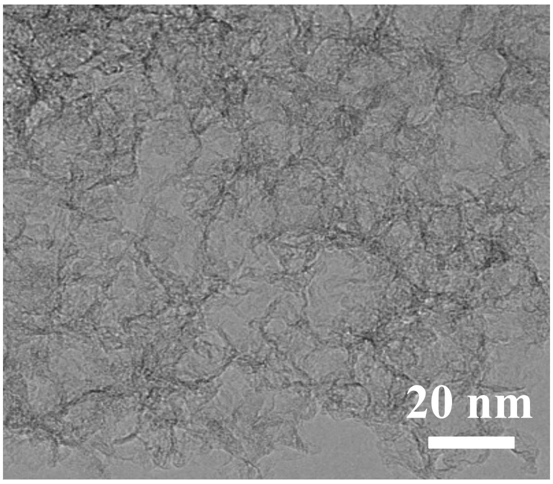

Fig. S5 HRTEM images of MC-NF.

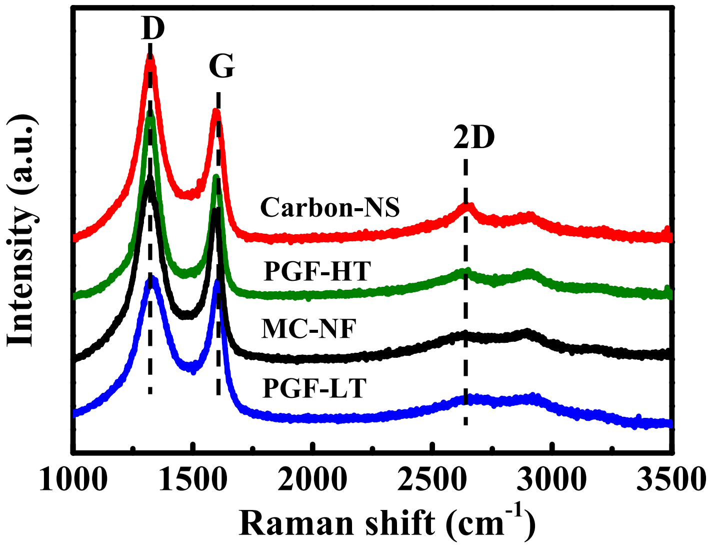

Fig. S6 Raman spectra of MC-NF, Carbon-NS, PGF-LT and PGF-HT.

The differences between the MC-NF, Carbon-NS, PGF-LT and PGF-HT are also probed by the observation in Raman spectra. As shown in Fig. S6, the MC-NF fabricated without ferrocene shows almost disappearing 2D band, indicating the essential role of catalytic graphitization by ferrocene. The similar Raman spectra of Carbon-NS to PGF disclose, once again, that colloidal silica only functioned as templates. Besides, for the samples prepared at lower or higher calcination temperature, the I_{2D}/I_G value of PGF-LT and PGF-HT was calculated to be 0.28 and 0.49 respectively, revealing reduced graphitization degree and thicker carbon layers than that of PGF with well-reserved porous frameworks consisted of three-six graphene layers.

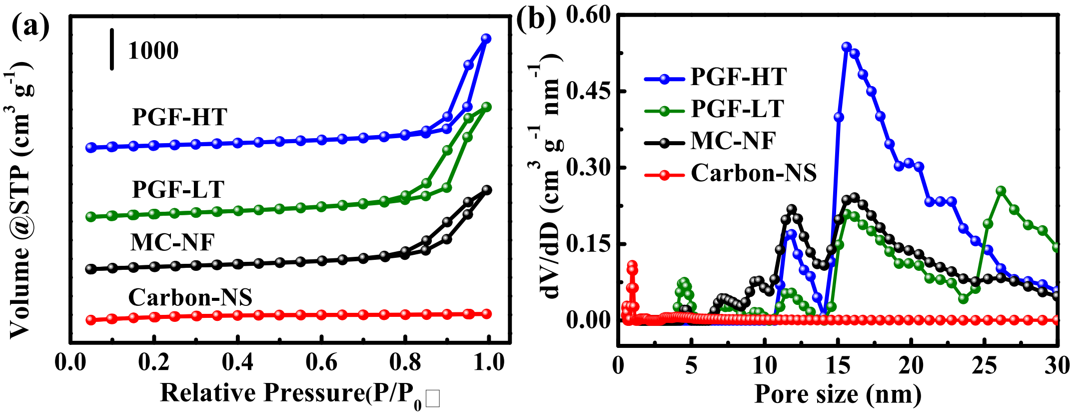

Fig. S7 (a) N_2 adsorption-desorption isotherms and (b) pore size distribution profiles of MC-NF, Carbon-NS, PGF-LT and PGF-HT.

The series of samples were subjected to the N_2 adsorption–desorption measurements to analyse the porosities, which are paramount for electrosorption. Obviously, MC-NF, PGF-LT and PGF-HT all share similar type-IV isotherm characteristics typical of a dominant mesoporous structures (Fig. S7a). The pore size distributions manifested in Fig. S7b determined dominating porous distribution peak at around 16 nm for MC-NF, PGF-LT and PGF-HT, which agree well with the size of silica templates and TEM observations. However, for Carbon-NS, the formation of homogeneous porous structures was impossible in the absence of colloidal silica templates. Carbon-NS only manifested a small number of micropores due to the function of gases such as CO_2 generated in the calcination process. The specific surface area for PGF, PGF- LT and PGF-HT were calculated to be 1219, 962 and 837 m^2 g^{-1} respectively. The thicker carbon shells can account for the reduced specific surface area of PGF-LT. A remarkable decrease of specific surface area of PGF-HT can be mainly attributed to the progressive collapse and aggregation of the superstructure. In addition, PGF exhibited a very high total pore volume of 5.13 cm^3 g^{-1}. Notably, when altering the carbonization temperature, the pore volume remarkably decreased to 3.63 cm^3 g^{-1}. Similarly, MC-NF (941 m^2 g^{-1}) and Carbon-NS (33 m^2 g^{-1}) also show a sensibly decreased specific surface area and pore volume compared to PGF with porous 3D few-layer graphene structures.

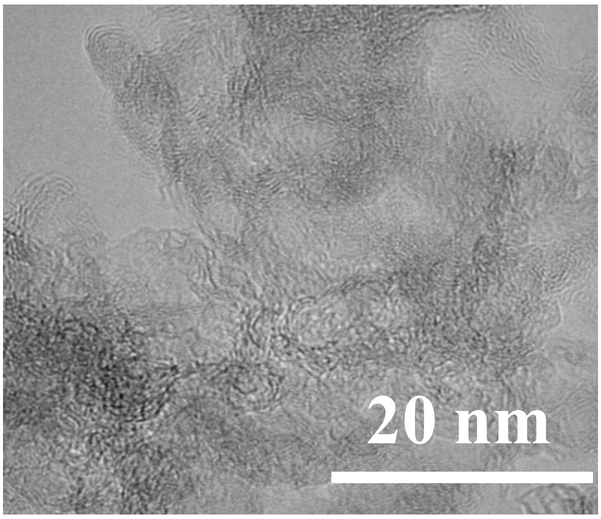

Fig. S8 HRTEM images of Carbon-NS.

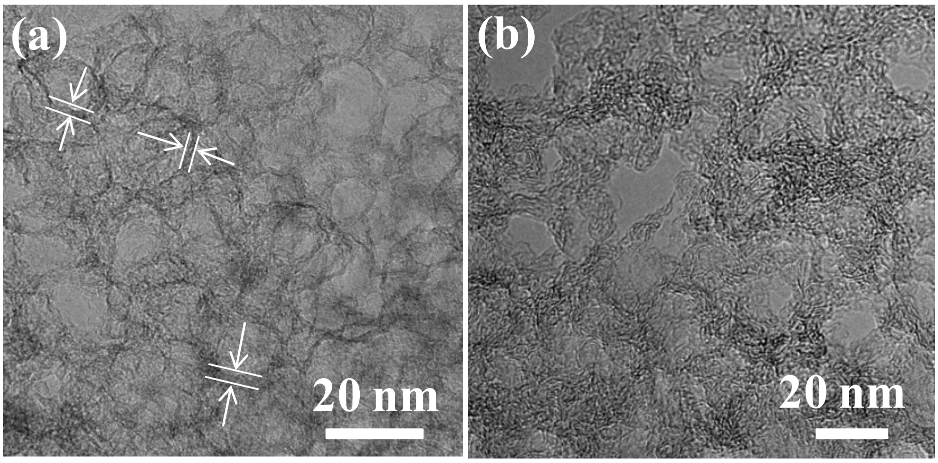

Fig. S9 HRTEM images of (a) PGF-LT and (b) PGF-HT.

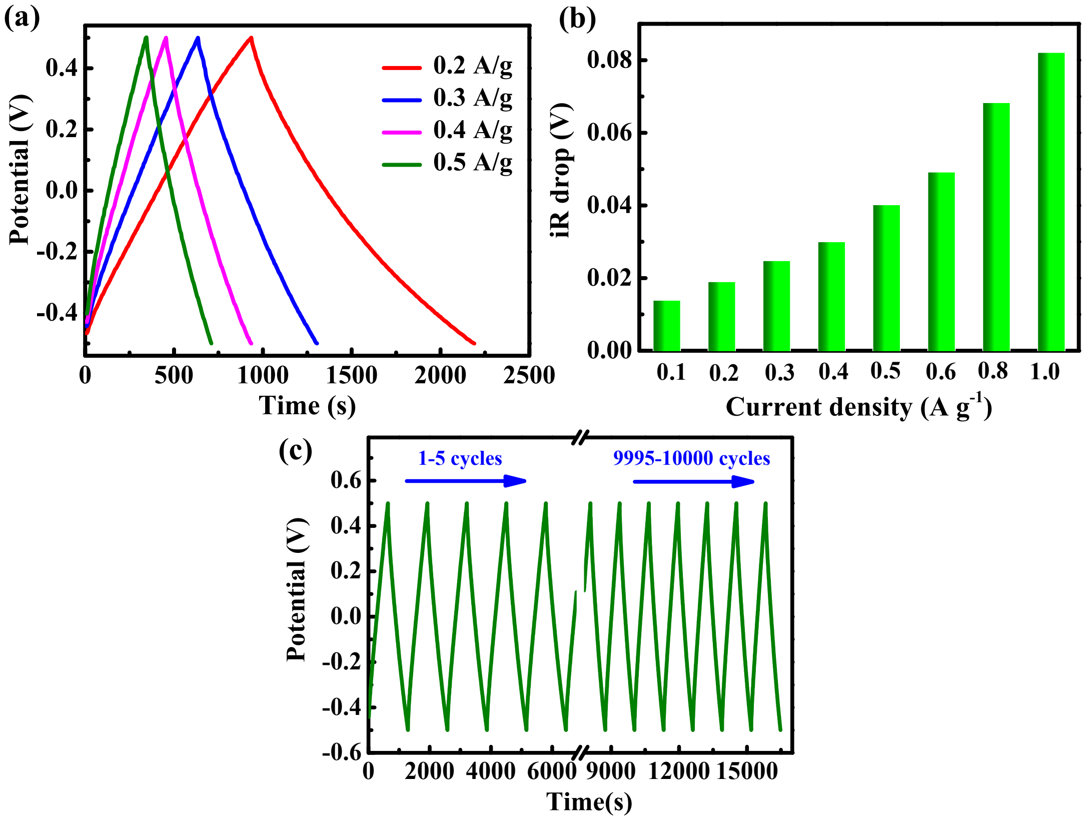

Fig. S10 (a) GCD curves at various current densities, (b) iR drop *vs.* current density and (c) Continuous GCD curves over10000 cycles at 0.3 A g^{-1} for the PGF electrodes. All the curves were obtained in a 0.5 M NaCl aqueous solution.

The GCD curves of PGF at different current densities were probed in Fig. S10a. It should be mentioned that the GCD curves all exhibit symmetric triangular shapes, revealing typical electric double layer behaviour and excellent electrochemical reversibility.[1] Significantly, for the PGF electrodes, almost linear potential–time plots in the whole potential range are observed for the GCD curves at different current densities, suggesting a fast I–V response during the adsorption process. Besides, the sudden voltage drop (iR drop) of PGF electrodes at the initial stage of discharge process can be used to reveal the inner resistance of electrode. As depicted in Fig. S10b, the iR drop at the low current density is inconspicuous, however, with the increase of current density, the value of iR drop increases due to the inadequate discharge in the electric double layer at the initial stage of discharge. Obviously, the smaller iR drop of

PGF reflects a smaller internal resistance, which agrees well with the above EIS results. This potentially accelerates the salty ions transport and diffusion across the 3D graphene conductive networks. Besides, as can be seen from the Fig. S10c, the PGF electrodes also reveal superior cycling stability with 97% capacitance retention after 10 000 cycles of continuous charge-discharge.

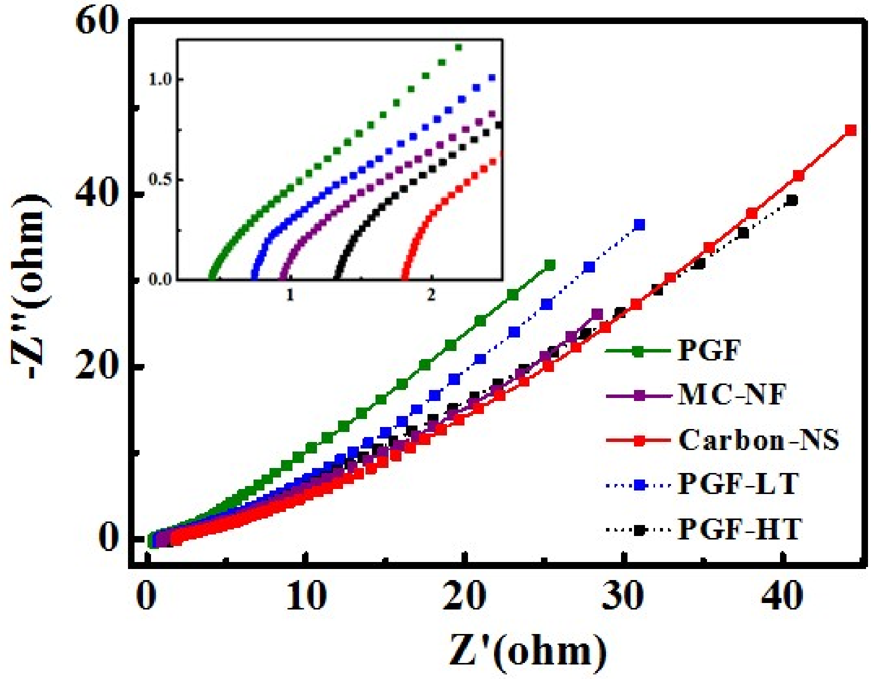

Fig. S11 Nyquist plots of PGF, MC-NF, Carbon-NS, PGF-LT and PGF-HT. The inset is the enlarged view of the high frequency region.

The ion diffusion kinetics and charge transfer in the electrosorption process of all electrodes were examined by EIS analysis. The Nyquist plots of PGF, MC-NF, Carbon-NS, PGF-LT and PGF-HT are plotted in Fig. S11. It can be vividly observed that all the Nyquist profiles present similar shapes and consist of a linear shape in the low frequency region and a small quasi-semicircle at the high frequency one.[2] The width of quasi-semicircles is generally in parallel with the charge transfer resistance (R_{ct}) between the electrode surface and solution. It should be noted that the R_{ct} of all electrodes are ignorable, suggesting the ultrasmall charge-transfer resistance. The point intersecting the real axis in Nyquist plots is the equivalent series resistance (ESR), which can be attributed to the contact resistance between the electrodes and current collectors, intrinsic electronic characteristics of the electrodes, the mass transfer resistance of ions as well as resistance of salt solution. A smaller ESR value generally indicates lower internal resistance and faster charge/discharge rate.[3] It can be obviously seen from the inset of Fig. S11 that the ESR value of PGF (0.44 Ω) is much smaller than those of MC-NF (0.90 Ω), Carbon-NS (1.83 Ω), PGF-LT (0.71 Ω) and PGF-HT

(1.30 Ω), indicating that the PGF electrode has lower resistance. In addition, the relatively straight line of all samples confirms primary contribution of electrostatic ion adsorption. It should be noted that the PGF possesses a more vertical line, suggesting better capacitor behavior due to the faster and more efficient ion transport and diffusion in the robust porous 3D few-layer graphene frameworks. In conclusion, the PGF electrode features lower internal resistance and superior electrical conductivity. This is because the 3D interconnected porous architectures and untrathin pore walls consisted of few-layer graphene can facilitate the efficient charge transfer and the ions diffusion.

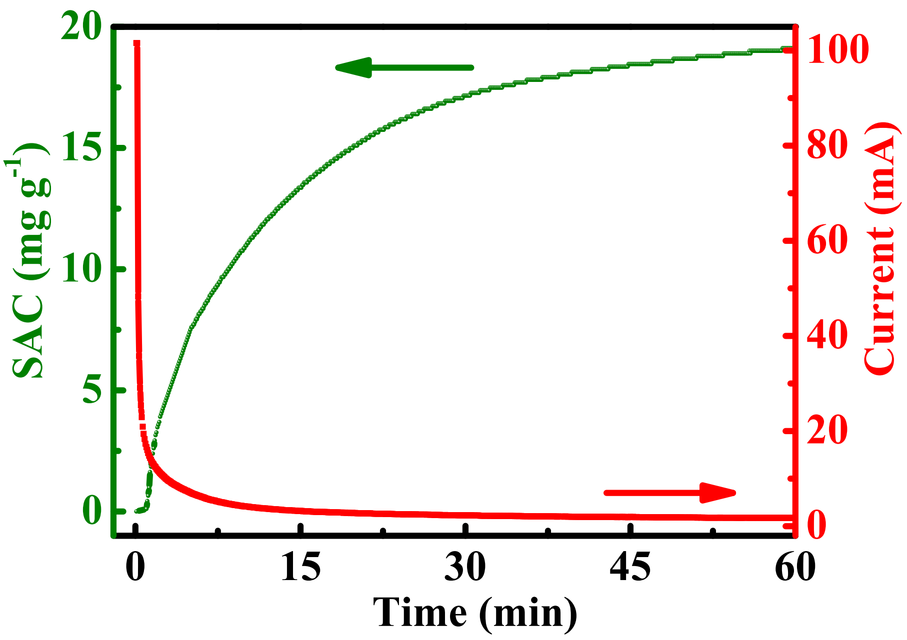

Fig. S12 Plots of current *vs.* time and SAC *vs.* time for the PGF electrodes in a 500 mg L^{-1} NaCl solution and at 1.4 V.

To get a better understanding of the electrosorption behaviour of PGF, the electrosorption experiments were carried out in a 500 mg L^{-1} NaCl solution and at 1.4 V. The corresponding plots of current *vs.* time and SAC *vs.* time for PGF are shown in Fig. S12. It can be seen that the corresponding SAC of PGF increased sharply at the initial stage, then increases slowly and even achieves stable with time going by. After 60 min, the SAC of PGF reaches significantly enhanced value of 19.1 mg g^{-1}. Further, the charge efficiency of PGF is calculated to be 0.57 according to equation (4), which suggested a lower energy consumption. Since the 3D porous conductive graphene networks across the PGF are beneficial to the electric double layer formation. However, the charge efficiency is below the theoretical value of 1.0, this is mainly caused by the following reasons: (i) the co-ion repulsion effect could result in lower charge efficiency. (ii) the weak adhesive attraction between the electrodes and current collector may account for the lower charge efficiency. (iii) the blocking influence of the binder can strengthen the resistance of the PGF electrodes and thus consume more voltage.

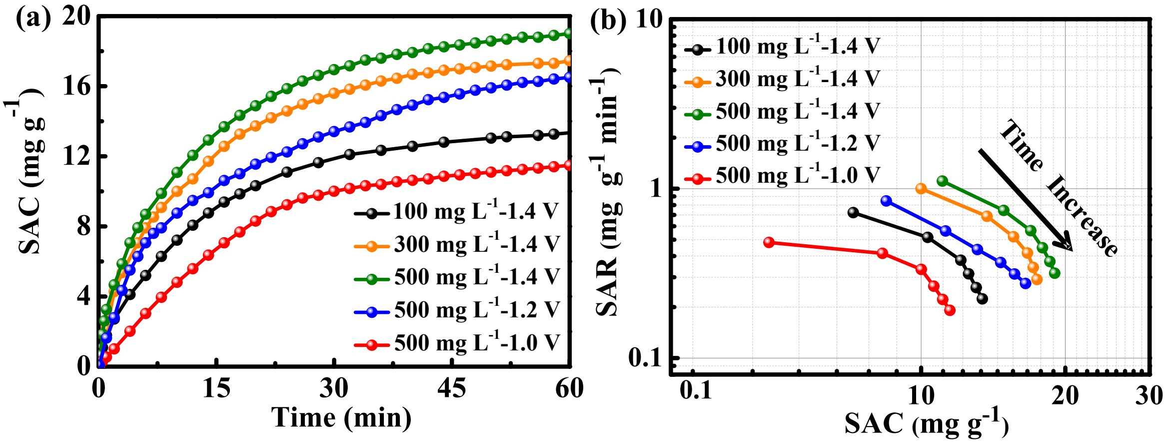

Fig. S13 (a) Plots of SAC *vs.* time and (b) Ragone plots of SAR *vs.* SAC for the PGF electrode under different concentration and voltage.

To get a better understanding of the electrosorption behavior of the PGF electrode, a series of electrosorption measurements were performed to verify the effects of prevalent parameters including voltage and salt concentration.[4] Fig. 13a depicts a series of electrosorption measurements for the PGF at different salt concentration and voltage. The plots of SAC *vs.* time under different concentration are firstly probed. For initial NaCl solution ranging from 100 to 500 mg L^{-1}, the SAC increases significantly once the voltage is introduced, and achieved adsorption equilibrium after about 60 min. The upward trend of SAC at a higher salt concentration is more obvious, demonstrating that more ions are electroabsorbed by the PGF electrode. It should be also noted that a higher salt concentration shifted the ragone plot toward the upper and righter region, revealing higher SAC and faster SAR (Fig. S13b). In addition, the increased SAR could be interpreted by the conductivity enhancement of the influent solution with higher concentration, accelerating swifter transport of ions into the electrodes. In this regard, a higher concentration of salt solution is favourable due to the formation of compact electric double layer and the subsequent accessible fast adsorption in comparison with a lower salt concentration. Next, the impact of applied voltage on electrosorption performance was also carefully examined. As seen in Fig. S13, the SAC increased to 19.1 mg g^{-1} when the voltage increased from 1.0 to 1.4 V. The corresponding Ragone plot was shifted to upward and right region when increasing the external voltage, indicating better electrosorption capacity and rate. At higher applied voltage, the easier ionic adsorption can be conducted due to the stronger coulombic interaction between charged ions and electrodes. These results confirm the strong influence of the applied voltage on the electrosorption performance, which is one of the crucial parameters when fabricating and optimizing an electrosorption process. In this work, at the external applied voltage of 1.4 V, no bubbles were observed due to the intrinsic resistance of the electrodes and solutions, which permits an overvoltage.[5]

Table S1 The specific surface area and pore volume for the investigated samples.

Sample	Specific Surface area (m^2 g^{-1})	Pore volume (cm^3 g^{-1})
PGF	1219	5.13
MC-NF	941	4.80
Carbon-NS	33	0.04
PGF-LT	962	4.91
PGF-HT	837	3.63

Table S2 Comparison of adsorption capacity of various carbon materials from the literature.

Electrode materials	Applied voltage [V]	Initial NaCl concentration [mg L^{-1}]	Adsorption capacity [mg g^{-1}]	Ref.
Graphene	2.0	250	4.60	6
Mesoporous graphene	1.6	~500	15.2	7
Nitrogen doped carbon aerogel	1.5	~1463	8.20	8
N-PHCS[a]	1.4	500	13.0	9
CFC-SRGO[b]	1.4	250	~8.07	10
Porous carbon spheres	1.6	500	5.81	11
Porous carbon spheres	1.4	50	~2.73	11
Carbon fibre cloths	1.4	250	~5.27	10
3D porous graphene	1.4	300	8.97	12
Porous Carbon Nanofibers	1.2	500	5.61	13
3D Graphene	1.4	500	9.48	14
PGF	1.4	500	19.1	This work
PGF	1.4	300	17.4	This work

[a] Nitrogen-doped porous hollow carbon spheres (N-PHCS)

[b] Carbon fibre cloth (CFC) and sulphonated reduced graphene oxide (SRGO) composites

References

1 J. Zhao, H. Lai, Z. Lyu, Y. Jiang, K. Xie, X. Wang, Q. Wu, L. Yang, Z. Jin, Y. Ma, J. Liu and Z. Hu, *Adv. Mater*, 2015, **27**, 3541.

2 (a) H. Wang, L. Zhi, K. Liu, L. Dang, Z. Liu, Z. Lei, C. Yu and J. Qiu, *Adv. Funct. Mater*, 2015, **25**, 5420; (b) T. Lin, I-W. C, F. Liu, C. Yang, H. Bi, F. Xu, F. Huang, *Science,* 2015, **350**, 1508.

3 Y. Liu, X. Xu, M. Wang, T. Lu, Z. Sun and L. Pan, *Chem. Commun*, 2015, **51**, 12020.

4 H. Wang, T. Yan, P. Liu, G. Chen, L. Shi, J. Zhang, Q. Zhong and D. Zhang, *J. Mater. Chem. A*, 2016, **4**, 4908.

5 (a) H. Lei, T. Yan, H. Wang, L. Shi, J. Zhang and D. Zhang, *J. Mater. Chem. A*, 2015, **3**, 5934; (b) P. Długołęcki and A. V. D. Wal, *Environ. Sci. Technol*, 2013, **47**, 4904.

6 B. Jia and L. Zou, *Chem. Phys. Lett*, 2012, **548**, 23.

7 X. Gu, M. Hu, Z. Du, J. Huang and C. Wang, *Electrochim. Acta*, 2015, **182**, 183.

8 G. Rasines, P. Lavela, C. Macías, M. C. Zafra, J. L. Tirado, J. B. Parra and C. O. Ania, *Carbon*, 2015, **83**, 262.

9 S. Zhao, T. Yan, H. Wang, G. Chen, L. Huang, J. Zhang, L. Shi and D. Zhang, *Appl. Surf. Sci,* 2016, **369**, 460.

10 H. Li, F. Zaviska, S. Liang, J. Li, L. He and H. Y. Yang, *J. Mater. Chem. A*, 2014, **2**, 3484.

11 Y. Liu, L. K. Pan, T. Q. Chen, X. T. Xu, T. Lu, Z. Sun and D. H. C. Chua, *Electrochim. Acta*, 2015, **151**, 489.

12 A. G. El-Deen, R. M. Boom, H. Y. Kim, H. Duan, M. B. Chan-Park and J.-H. Choi, *ACS Appl. Mater. Inter,* 2016, **8**, 25313.

13 J. Liu, Z. Xiong, S. Wang, W. Cai, J. Yang and H. Zhang, *Electrochim. Acta*, 2016, **210**, 171.

14 P. Liu, H. Wang, T. Yan, J. Zhang, L. Shi and D. Zhang, *J. Mater. Chem. A*, 2016, **4**, 5303.